






## RESEARCH ARTICLE

# Daily and seasonal variation of the surface temperature lapse rate and 0°C isotherm height in the western subtropical Andes

María Ibañez<sup>1</sup>  | Jorge Gironás<sup>1,2,3,4</sup>  | Christian Oberli<sup>2,5</sup>  |  
Cristián Chadwick<sup>6</sup>  | René D. Garreaud<sup>7,8</sup> 

<sup>1</sup>Departamento de Ingeniería Hidráulica y Ambiental, Pontificia Universidad Católica de Chile, Santiago, Chile

<sup>2</sup>Centro de Investigación para la Gestión Integrada del Riesgo de Desastres, CONICYT/FONDAP/15110017, Santiago, Chile

<sup>3</sup>Centro de Desarrollo Urbano Sustentable, CONICYT/FONDAP/15110020, Santiago, Chile

<sup>4</sup>Centro Interdisciplinario de Cambio Global, Pontificia Universidad Católica de Chile, Santiago, Chile

<sup>5</sup>Departamento de Ingeniería Eléctrica, Pontificia Universidad Católica de Chile, Santiago, Chile

<sup>6</sup>Facultad de Ciencias Forestales y de la Conservación de la Naturaleza, Universidad de Chile, Santiago, Chile

<sup>7</sup>Departamento de Geofísica, Universidad de Chile, Santiago, Chile

<sup>8</sup>Centro de Ciencia del Clima y la Resiliencia, Universidad de Chile, Santiago, Chile

## Correspondence

Jorge Gironás, Departamento de Ingeniería Hidráulica y Ambiental, Pontificia Universidad Católica de Chile, Santiago, Chile.  
Email: jgironas@ing.puc.cl

## Funding information

Fondo de Financiamiento de Centros de Investigación de Áreas Prioritarias, Grant/Award Numbers: 15110009, 15110017, 15110020; Fondo de Fomento al Desarrollo Científico y Tecnológico, Grant/Award Number: IT13i20015; Fondo Nacional de Desarrollo Científico y Tecnológico, Grant/Award Number: 1161439

## Abstract

The spatial distribution of surface air temperatures is essential for understanding and modelling high-relief environments. Good estimations of the surface temperature lapse rate (STLR) and the 0°C isotherm height (H0) are fundamental for hydrological modelling in mountainous basins. Although STLR changes in space and time, it is typically assumed to be constant leading to errors in the estimation of direct-runoff volumes and flash-floods risk assessment. This paper characterizes daily and seasonal temporal variations of the in-situ STLR and H0 over the western slope of the subtropical Andes (central Chile). We use temperature data collected during 2 years every 10 min by a 16 sensors network in a small catchment with elevations ranging between 700 and 3,250 m. The catchment drains directly into Santiago, the Chilean capital with more than seven million inhabitants. Resulting values are compared against those obtained using off-site, operational data sets. Significant intra- and inter-day variations of the in-situ STLR were found, likely reflecting changes in the low-level temperature inversion during dry conditions. The annual average in-situ STLR is  $-5.9^{\circ}\text{C}/\text{km}$  during wet-weather conditions. Furthermore, STLR and H0 estimations using off-site gauges are extremely sensitive to the existence of gauging stations at high elevations.

## KEYWORDS

Chile, 0°C isotherm, high density sensor network, mountains, temperature lapse rate, warm events

## 1 | INTRODUCTION

Surface air temperature (SAT, normally measured at 2 m above the surface) and its spatial distribution are key climatic features in mountainous regions (Yang *et al.*, 2011; Wang *et al.*, 2017), essential for understanding and modelling a wide range of processes in high-elevation environments (Minder *et al.*, 2010; Pages *et al.*, 2017; Ojha, 2019). In particular, the relationship between SAT and altitude, that is, the surface temperature lapse rate (STLR), controls some relevant processes such as rainfall-runoff transformation, snow accumulation and snowmelt, ecosystems distributions and glacier mass variations. An accurate estimation of the STLR is crucial in mountainous regions (Rolland, 2003; Blandford *et al.*, 2008; Kattel *et al.*, 2013, 2015, 2018). Closely related to the STLR is the 0°C isotherm height (H<sub>0</sub>), a very relevant variable in mountain hydrology that approximately delimitates the area that produces direct runoff and the area that receive snow (White *et al.*, 2002; Lundquist *et al.*, 2008; Minder *et al.*, 2010; Garreaud, 2013; Immerzeel *et al.*, 2014).

Hydrological modelling and other applications commonly use STLR to extrapolate SAT from a low-lying base station to different elevations with no observations (Blandford *et al.*, 2008; Ojha, 2019). Typical STLR values range between  $-7.0$  and  $-6.0^{\circ}\text{C}/\text{km}$  (Prentice *et al.*, 1992; Hamlet and Lettenmaier, 2005; Otto-Bliesner *et al.*, 2006; Livneh *et al.*, 2013; Ojha, 2019), with  $-6.5^{\circ}\text{C}/\text{km}$  being most commonly used (Blandford *et al.*, 2008; López-Moreno *et al.*, 2018). This value corresponds to the standard atmospheric lapse rate representative of the theoretical pseudoadiabatic lapse rate (Brunt, 1933). However, this value is often adopted without in-situ observational support and may result inappropriate in many circumstances (Minder *et al.*, 2010). Note that free-air temperature lapse rate (FTLR) and STLR differ, particularly in mountains regions, as the heated or cooled land surface is essentially projected into the free air with the form of mountains (Blandford *et al.*, 2008). Thus, the STLR is expected to be more variable than the FTLR. Moreover, the STLR is known to vary in time and space, especially in complex terrains (Minder *et al.*, 2010; Pike *et al.*, 2013; Ojha, 2017; Wang *et al.*, 2017). This variability has been studied in different regions by using observational temperature sensor networks (Minder *et al.*, 2010; Pike *et al.*, 2013) and satellite estimates of SAT (González and Garreaud, 2019). Some of the studies include seasonal (Bolstad *et al.*, 1998; Rolland, 2003; Tang and Fang, 2006; Blandford *et al.*, 2008) and diurnal cycles (Bolstad *et al.*, 1998; Rolland, 2003; Tang and Fang, 2006; Blandford *et al.*, 2008; Wang *et al.*, 2017), as well as the spatial variability of the STLR (Bolstad *et al.*, 1998; Pepin, 2001; Rolland, 2003; Tang and

Fang, 2006; Minder *et al.*, 2010; Kattel *et al.*, 2013; López-Moreno *et al.*, 2018).

Mountainous terrain provides many challenges for the installation and maintenance of meteorological instruments (Chae *et al.*, 2012). The number of available weather stations in a mountainous region is often insufficient for the complete coverage of the altitude ranges (Rolland, 2003; Wang *et al.*, 2017). Nevertheless, dense sensor networks with high temporal resolution are key to describe how local STLR evolves through time (Lundquist and Cayan, 2007; Minder *et al.*, 2010; Ojha, 2017). Attaining such knowledge improves our understanding of temperature patterns in mountainous regions, as well as the overall characterization of mountain climates. Some high-relief regions in which STLR have been measured and characterized are the Himalayas (Kattel *et al.*, 2013, 2015, 2018), the Qinling mountains of China (Tang and Fang, 2006; Wang *et al.*, 2017), the BaekduDaegan Mountain of Korea (Chae *et al.*, 2012), the European Alps (Rolland, 2003), the Rocky Mountains (Blandford *et al.*, 2008), Cascade Mountains (Minder *et al.*, 2010) in North America, the Mountainous British Columbia (Cannon *et al.*, 2012) and the Nahuelbuta coastal mountains in southern Chile (González and Garreaud, 2019). It stands out that the Andes Mountains along western South America have received relatively little attention in this respect. To the best of our knowledge, studies of SAT distribution exist only for the Ecuadorian tropical Andes (Córdova *et al.*, 2016) and for some specific glaciers in the Chilean Andes (Petersen and Pellicciotti, 2011; Hanna *et al.*, 2017), and rely on less than 1 year of records. As we will show, longer periods of observation do provide valuable insight into the STLR variation from one season to another.

This paper presents an empirical study to characterize the temporal dynamics of the STLR and H<sub>0</sub> in the western side of the subtropical Andes ( $33\text{--}34^{\circ}\text{S}$ ). The study zone is located in the Maipo River basin, a major basin in central Chilean where both liquid and solid precipitation are relevant (Garreaud, 2013). Understanding the STLR in this region is of high interest because the seasonal snowpack during winter and some glaciers provide water supply for this semiarid environment (Pellicciotti *et al.*, 2014). Moreover, Santiago, the capital of the country, is located at the foothills of the Andes, thus exposed to flash floods and landslides (Lara *et al.*, 2018) that can be triggered by winter warm storms with an elevated H<sub>0</sub> (Garreaud, 2013). Here, we take advantage of a wireless sensor network of 16 stations deployed in a small catchment at the eastern edge of Santiago, with elevations ranging from  $\sim 700$  to 3250 m above sea level (ASL), which measured SAT every 10 min during a 2-year period (2016–2018). H<sub>0</sub> and the seasonal and diurnal STLR

cycles are studied, as well as the STLR behaviour during wet- and dry-weather conditions. These results are compared against estimations using off-site weather stations data and FTLR estimated from nearby atmospheric sounding data.

The paper is organized as follows. Section 2 is a background section presenting the climate context and details of the study area. Section 3 presents the data and analysis methods. Results with a focus on the characterization and comparison among the different sources are presented in Section 4, while Section 5 illustrates the hydrological implications associated with the different STLR and H0 estimations. Finally, Section 6 comprises a summary and the main conclusions.

## 2 | BACKGROUND

### 2.1 | Climate context

The subtropical Andes (30–35°S, Figure 1) reach more than 5,000 m ASL and exhibit a complex terrain with steep slopes and deep canyons covered by sparse vegetation (Comin *et al.*, 2018). The climate of the western side of Andes at subtropical latitudes (Central Chile) is classified as semiarid, Mediterranean (Kottek *et al.*, 2006; Peel *et al.*, 2007; Garreaud *et al.*, 2009), with a cold and rainy season from May to September, and a warm and extremely dry season from October to April. Average rainfall in the city of Santiago (550 m ASL) is 310 mm/year, but precipitation increases markedly over the mountainous terrain reaching ~1,300 mm/year atop of the Andes (Viale and Garreaud, 2015). This region exhibits substantial year-to-year variability with a *SD* to mean ratio of about 0.3 (Garreaud *et al.*, 2017; their Figure 1). Such interannual variability is largely modulated by the El Niño Southern Oscillation (ENSO): wet winters tend to occur during El Niño years while droughts are more frequent during La Niña years (Montecinos and Aceituno, 2003; Oertel *et al.*, 2020). Drier than normal conditions, however, have prevailed during the last decade (the central Chile mega drought, Garreaud *et al.*, 2017) under ENSO-neutral conditions signalling the early effects of the climate change in this region.

Precipitation events during winter are mostly caused by passage of cold fronts rooted in extratropical cyclones (Falvey and Garreaud, 2007). Consequently, most of the winter storms are accompanied by cold air temperatures (with respect to dry days) that lowers H0 to about 2,300 m ASL, thus causing snow accumulation in the upper part of the Andes. Upper-level cyclonic vortices

detached from the polar jet (cut-off lows) can also deliver some precipitation in this area (Fuenzalida *et al.*, 2005) but are rather infrequent (less than 7–10 events per year). Even more uncommon are precipitation events during summer caused by convective storms atop of the Andes that produce rainfall only at higher elevations (Viale and Garreaud, 2014). During the wet season, heavy and extreme precipitation events are associated with Atmospheric Rivers (AR), in which a narrow band of moist laden air impinges directly against the Andes (Viale *et al.*, 2018; Valenzuela and Garreaud, 2019). Some of these ARs develop with rather warm air temperatures—the so-called warm winter storms (Garreaud, 2013)—during which H0 remains high (i.e., >3,000 m ASL, sometimes as high as 4,000 m ASL). The combination of strong precipitation and an elevated H0 results in very hazardous conditions and can lead to extensive flooding (Garreaud, 2013) and/or more localized flash floods (Lara and Sepúlveda, 2010; Castro *et al.*, 2019) in central Chile.

### 2.2 | Study area

The study region is framed in the Maipo River basin, located in central Chile (Figure 1a) between 32°55'S–34°15'S and 69°46'–71°43'W. This basin has an area of 15,304 km<sup>2</sup> and extends from sea level up to 6,500 m ASL in the western side of the Andes (Figure 1b). The Maipo River provides water supply for the environment and for a variety of uses such as agriculture, mining industry (Pellicciotti *et al.*, 2014) and drinking water of ~1,440,000 households (Sarmiento *et al.*, 2019) corresponding to 60% of the households in the metropolitan area (SISS, 2018). The basin hosts Santiago, the Chilean capital, with more than seven million inhabitants in the metropolitan area (approximately 40% of the nation's population) (INE, 2018). During past decades, the city has grown towards the Andes foothills (Romero *et al.*, 1999; Pávez *et al.*, 2010; Sanzana *et al.*, 2019), where more than 30 sub-catchments are drained by ravines and gullies forming alluvial fans, posing an increasing risk to population (Lara *et al.*, 2018). These ravines are in the western slope of Andes mountains, known as “Pre-Cordillera,” where the highest altitude (3,250 m ASL) is the San Ramón hill in the Quebrada de Ramón catchment (Sepúlveda and Padilla, 2008).

Floods, debris flows and mudflows are common in the area, and their modelling and forecasting rely strongly on the STLR. More than 15 of these events affecting thousands of people have occurred since 1980, causing 80 fatalities and material losses exceeding 17.5 million USD (Sernageomin, 2007). The event of May 3, 1993, occurred under abnormal conditions of the 0°C

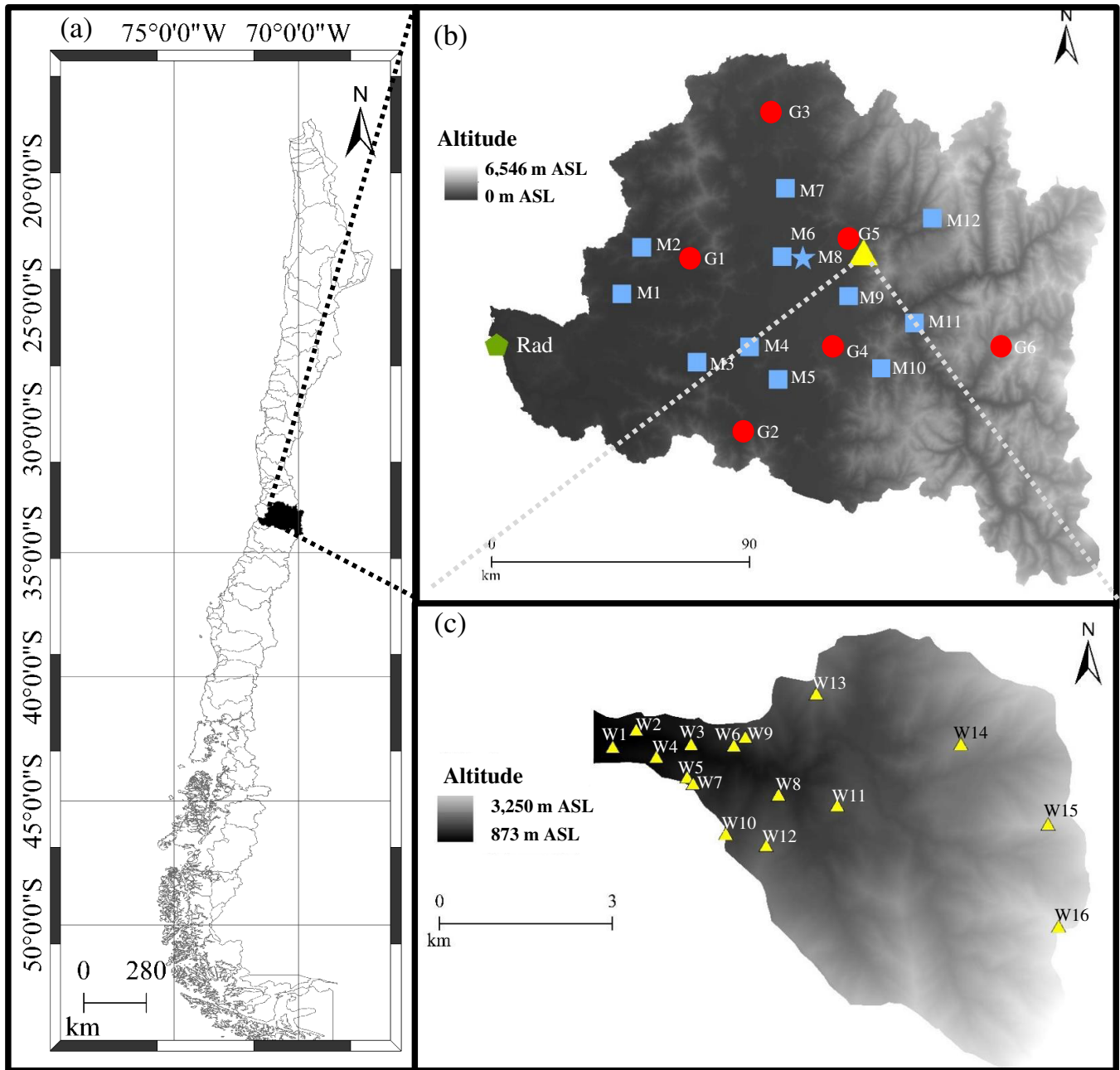


**FIGURE 1** Chile (a), the Maipo River basin (b) and the Quebrada de Ramón catchment (c). The yellow triangles are the WSN stations (W), the light blue squares are the DMC stations (M), and the star represents the Quinta Normal station. The red circles are the DGA stations (G). The Santo Domingo radiosonde launched location is denoted with a green pentagon [Colour figure can be viewed at [wileyonlinelibrary.com](http://wileyonlinelibrary.com)]

isotherm, whose elevation rose up to  $\sim 4,000$  m ASL due to high temperatures during the event (Garreaud & Rutllant 1997; Sepúlveda and Padilla, 2008). For this event debris floods occurred in two ravines located in the foothills of Santiago: Quebrada de Macúl and Quebrada de Ramón. The catchment contributing to the later has a total area of  $39.5 \text{ km}^2$  and elevations ranging between 700 and 3,250 m ASL, and it corresponds to the study area of this study (Figure 1c).

### 3 | DATA AND METHODS

#### 3.1 | Data sets

Four data sets are used in this work. The first data set is from a wireless sensor network (referred to henceforth as WSN) deployed by our group in Quebrada de Ramón catchment just east of Santiago (Figure 1c). Two other sets of surface records were obtained from permanent

networks operated by the Chilean Weather Office (DMC, Dirección Meteorológica de Chile) and Chilean General Water Office (DGA, Dirección General de Aguas). DMC also provides atmospheric profiles measured by radiosondes launched daily at Santo Domingo, a coastal station at the same latitude of Santiago.

The WSN is composed of 16 micro-stations located at elevations between 878 and 2,962 m ASL (Table 1), with 10 of them located between 1,000 and 2,000 m ASL, and 3 above 2,000 m ASL. Such vertical range encompasses the typical altitude of the 0°C isotherm in central Chile during winter storms (2,300 m ASL  $\pm$ 500 m; Garreaud, 2013).

**TABLE 1** Identification, latitude, longitude and elevation of the WSN (W), DMC (M) and DGA (G) meteorological stations

ID	Name	Latitude (S)	Longitude (W)	Elevation (m ASL)	Aspect
W1	Acumulador QR	33°25'48"	70°31'12"	878	SW
W2	Reforestación <sup>a</sup>	33°25'48"	70°30'36"	947	SW
W3	Diego	33°25'48"	70°30'0"	999	S
W4	Estanque	33°26'24"	70°30'36"	1,002	NE
W5	QR04	33°26'24"	70°30'0"	1,166	N
W6	Repetidor Los Peumos	33°25'48"	70°29'24"	1,228	S
W7	QR05	33°26'24"	70°30'0"	1,236	N
W8	Repetidor Confluencia	33°26'24"	70°29'24"	1,338	N
W9	Repetidor los Peumos 2	33°25'58"	70°29'28"	1,354	SW
W10	QR07	33°27'0"	70°30'0"	1,472	E
W11	Repetidor Apoquindo	33°26'24"	70°28'12"	1,573	W
W12	QR08	33°27'0"	70°29'24"	1,706	NE
W13	Alto las Vizcachas	33°25'48"	70°28'48"	1,752	S
W14	Provincia Bajo <sup>a</sup>	33°25'48"	70°27'0"	2,117	W
W15	Tambor Bajo	33°27'0"	70°26'24"	2,627	SW
W16	Mirador Los Maquis	33°27'36"	70°25'48"	2,962	N
M1	Chorombo Hacienda	33°31'48"	71°13'48"	145	
M2	Curacaví Ad.	33°24'36"	71°10'12"	208	
M3	El Paico	33°42'36"	71°0'36"	275	
M4	Talagante	33°40'12"	70°50'60"	390	
M5	El Milagro, Buin	33°45'0"	70°45'36"	460	
M6	San Pablo-DASA	33°26'24"	70°45'0"	490	
M7	Lo Pinto	33°16'12"	70°43'48"	512	
M8	Quinta Normal	33°27'0"	70°40'48"	534	
M9	Aguas Andinas	33°32'60"	70°32'60"	670	
M10	Rio Clarillo	33°43'12"	70°29'24"	876	
M11	San José Guayacán	33°37'12"	70°20'60"	928	
M12	El Colorado	33°21'0"	70°17'24"	2,750	
G1	Los Panguiles	33°26'24"	71°1'48"	190	
G2	Laguna Aculeo	33°53'24"	70°52'48"	360	
G3	Huenchun Andina	33°4'12"	70°46'48"	590	
G4	Pirque	33°40'12"	70°35'24"	659	
G5	Cerro Calán	33°23'60"	70°32'24"	848	
G6	Yeso	33°40'48"	70°5'24"	2,475	
Rad	Santo Domingo Radiosonde	33°38'60"	71°36'36"	—	

Note: Temperature is measured in all the Stations.

<sup>a</sup>Stations that also measure precipitation.

Each station has sensors to measure one or several variables of interest (e.g., air temperature, humidity, rainfall among others) every 10 min, a processor that controls the sensors and communication with the other micro-stations, and a radio to wirelessly send the measurements to a micro-station designated as accumulator. Because the stations use solar panels, they are all well exposed with the panels oriented to the north; moreover, temperature sensors are installed inside a Stevenson screen. Figure 2 shows three examples of the WSN stations at low, middle and high elevations, while Table 1 also indicates the aspect of the hill slopes where they are located. Two years of WSN temperature records from September 2016 to August 2018 were used in our analysis. Although the cumulative precipitation in the winters of 2017 and 2018 was below than average, the deficit was not extreme (20–25%). Likewise, the annual temperature for these years was within  $0.5^{\circ}\text{C}$  of the long-term average (1980–2010). Furthermore, the Oceanic Niño Index reported by NOAA was mostly neutral, with some cold anomalies not strong enough to call a “Niña” phase. Therefore, we feel confident that our observational record should describe the typical conditions in central Chile.

While the high resolution of WSN data is very suitable to estimate STLR and  $H_0$ , we contrast these results against DMC and DGA data because these operational records are long and freely available, and widely used in hydrological studies in central Chile. DMC has 13 operational automatic weather stations in the Maipo basin (Figure 1b), located at elevations between 145 and 2,750 m ASL, measuring temperature at a frequency of 1 min air since December 2016. As the DMC is an official state agency, the installation of the temperature sensors followed an official protocol (Maldonado *et al.*, 2010), which defines an elevation of 2 m above the ground, and the use of a Stevenson screen to avoid the influence of solar radiation and protect the instrument from rain,

dew, among others. One station (Lo Prado) was left out of the study due to its location in the coastal range. The highest DMC station (El Colorado, 2,750 m ASL) operates since January 2017. On the other hand, DGA has 41 hydrometeorological stations in the Maipo River basin. In the study, we use the six of them that regularly record maximum and minimum daily temperatures ( $T_{\max}$  and  $T_{\min}$ ), which are located at elevations ranging between 190 and 2,567 m ASL (Figure 1b). Note that none of the DMG and DGA stations is located in the 1,000–2,000 m ASL band. Further information on the DMC and DGA stations used in the study is presented in Table 1.

Finally, tropospheric air temperatures were obtained from radiosonde data launched twice daily (00 and 12 UTC; Local time = UTC-4) at Santo Domingo ( $34^{\circ}4'48''\text{S}$ – $72^{\circ}00'36''\text{W}$ ) by the DMC. This is a coastal station about 110 km to the west of the Quebrada de Ramón (Figure 1), so the sounding measurements are representative of the atmosphere encompassing the Maipo River basin (Roney, 2007; Yáñez-Morrón *et al.*, 2018). Furthermore, the prevailing westerly winds move the sonde towards the Andes during its ascent.

### 3.2 | Data pre-processing

The WSN and the DMC data sets were pre-processed to remove outliers and duplicated measurements, and to establish a common and regular time basis. Temperature outliers were eliminated using a filter to detect sudden changes and excessive oscillations, as the temperature is not expected to change much within 10 min time intervals. For precipitation data, outliers were considered to be the magnitudes exceeding 15 mm in 10 min, roughly twice the 100-year return period, 10-min rain in the area (PHI-LAC, 2013). Finally, linear and cubic interpolations

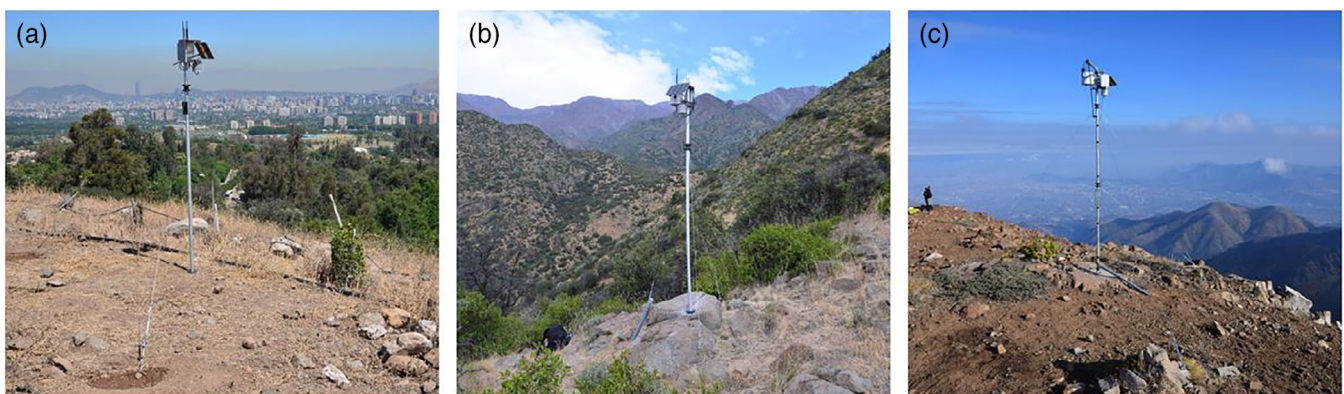


**FIGURE 2** WSN meteorological station at different altitudes, (a) W1 at 878 m ASL, (b) W8 at 1,338 m ASL and (c) W14 at 2,627 m ASL [Colour figure can be viewed at [wileyonlinelibrary.com](http://wileyonlinelibrary.com)]

were used to ensure a constant time step of the temperature and cumulative precipitation series. These interpolations allowed the filling of missing data in gaps of up to 30 min, larger gaps were not filled. Furthermore, the 1 min DMC temperature series were resampled instantaneously using a time step of 10 min (i.e., the time step of the WSN data set). After that, we smoothed both series with central moving average. These series are used for all the subsequent calculations.

Finally, daily  $T_{\max}$  and  $T_{\min}$ , and average temperatures ( $T_{\text{avg}}$ ) were extracted from the smoothed 10-min WSN and DMC series. Shorter time resolution will make  $T_{\max}$  and  $T_{\min}$  more extreme; nonetheless using a time step of 1 min, 10 min or 1 h has a negligible effect in the estimation of STLR for the DMC dataset, as shown in the Supporting Information (Figure S1). On the other hand, daily  $T_{\max}$  and  $T_{\min}$  are precisely the values reported in the DGA data set, whereas  $T_{\text{avg}}$  values were obtained as the average between  $T_{\max}$  and  $T_{\min}$ .

### 3.3 | Estimation of surface temperature lapse rates and 0°C isotherm

STLR and H0 were estimated from the WSN dataset every 10 min. For a given time, these calculations were performed only when temperature measurements from five or more stations were available (a time report by month of each WSN station is presented in the Figure S2 of the Supporting Information to illustrate the robustness of our decision). The STLR corresponds to the resulting slope of the simple linear regression using all available temperature values at that time. This STLR calculated from WSN dataset will be hereafter referred to as the in-situ STLR. Negative STLR values imply the typical case in which temperature decreases with height. Because all the temperature data at different elevations are used in the linear regression, less negative values of STLR and low associated determination coefficient ( $R^2$ ) coefficients are expected when thermal inversion takes place.

To obtain H0 two cases were considered:

- If H0 is located between the lowest and highest stations, its altitude is estimated from the linear interpolation between the consecutive stations recording temperatures above and below 0°C. In a few cases, a thermal inversion layer produced two such conditions, cases in which we interpolate between the pair of stations located at higher altitudes.
- If H0 is located outside the vertical range covered by the stations (878 and 2,962 m ASL), its altitude is estimated from the extrapolation of the linear regression according to the in-situ STLR. Due to the precision of

the temperature gauge ( $\pm 0.3^\circ\text{C}$ ), and regardless of the distance of the extrapolation, a Monte Carlo analysis determined that an error H0 are restricted to  $\pm 20$  m during 90% of the time, as long as H0 is under the maximum elevation in the sub-catchment (3,250 m ASL), which is the typical case.

We proceeded in the same fashion as above to estimate STLR using the DMC temperature series. To find H0, a linear regression as described in case (a) was used. Moreover, a second estimation of H0 based on DMC temperature series was that obtained using constant lapse rates varying between  $-8$  and  $-4^\circ\text{C}/\text{km}$  every  $0.5^\circ\text{C}/\text{km}$ , and the Quinta Normal (DMC) weather station as a reference (station M8, Table 1). This station located in Santiago (534 m ASL) and operating since 1911 is widely used as the reference station in local hydrological studies, in which H0 is estimated after assuming a constant lapse rate.

For the DGA data set, three daily STLR using linear regressions fitted independently to the sets of  $T_{\max}$ ,  $T_{\min}$  and  $T_{\text{avg}}$  values were estimated. A minimum of three data points was required for these fits. H0 was estimated by interpolating or extrapolating the fitted linear regression. Finally, the FTLR was estimated using the Santo Domingo soundings by simple linear regression of the temperature profile. H0 was calculated by direct linear interpolation of the last and first altitude values reported by the radiosonde above and below 0°C. Inversion layers are typically observed during dry conditions but they are warm and located near the surface so they do not affect the interpolation of the freezing level. During wet episodes, the temperature profile closely follows the saturated adiabat and the identification of the freezing level results unequivocal.

## 4 | RESULTS

### 4.1 | Monthly and hourly STLR

Figure 3 compares the monthly average of the in-situ STLR and the STLR from the DMC and DGA data sets calculated using daily values of  $T_{\max}$ ,  $T_{\min}$  and  $T_{\text{avg}}$ . In agreement with reports for other mountainous locations (Bolstad *et al.*, 1998; Rolland, 2003; Blandford *et al.*, 2008; Minder *et al.*, 2010), monthly mean STLR values calculated with  $T_{\max}$  are the steepest (i.e., temperature decreases the most with elevation), regardless of the data set used in the calculation. We interpret this result as a consequence of the common occurrence of low-level temperature inversions over central Chile (Garreaud and Rutllant, 2004; Muñoz and Undurraga, 2010) during

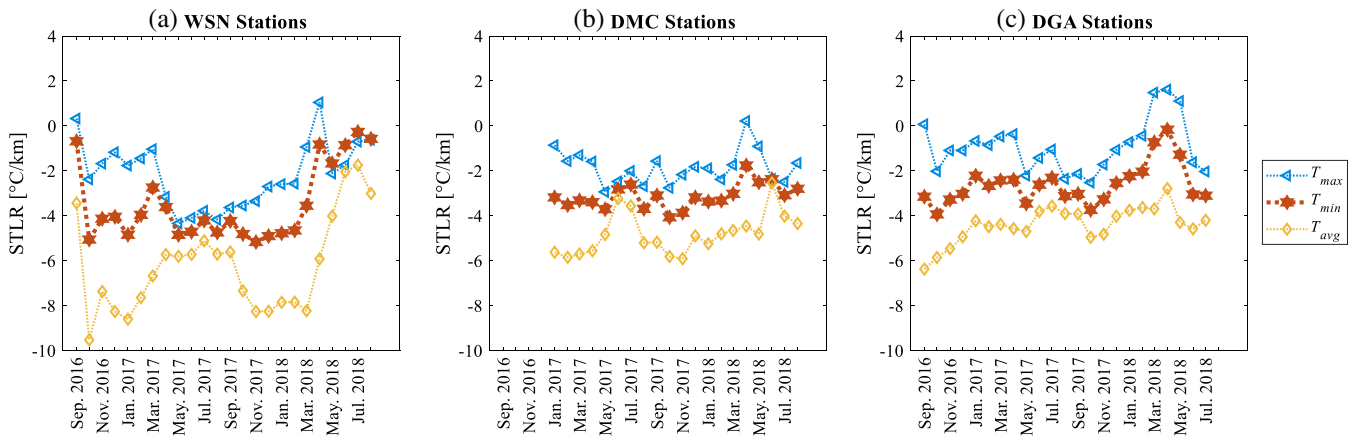


**FIGURE 3** WSN meteorological station at different altitudes, (a) W1 at 878 m ASL, (b) W8 at 1,338 m ASL and (c) W14 at 2,627 m ASL [Colour figure can be viewed at [wileyonlinelibrary.com](http://wileyonlinelibrary.com)]

night time and early morning hours. Since the in-situ STLR is the fitted slope of SAT using all stations, an inversion layer (temperature increase with height) tends to reduce the lapse rate. As the surface heating destroys the inversion by turbulent mixing, the STLR increases, which is consistent with the steepest value found when using  $T_{\max}$  (usually recorded in the afternoon). Furthermore, monthly STLR values estimated with the DMC and DGA (Figure 3b,c) data sets vary less in time than those estimated with the WSN data set (Figure 3a), that is, the  $SDs$  associated with  $T_{\max}$  are 1.9, 0.8, and  $2.4^{\circ}\text{C}/\text{km}$ , respectively. Monthly values estimated with  $T_{\max}$ ,  $T_{\min}$  and  $T_{\text{avg}}$  tend to be more similar between May and August (the coldest and rainy season) for all the data sets, reflecting the less marked diurnal cycle of surface temperature and the maintenance of the inversion layer during the day. Significant differences between the STLR values for the same month but different years are observed, especially for the WSN data set during May–July. These differences largely reflect changes in the frequency and intensity of temperature inversions, and may be due to synoptic changes. Nevertheless, a longer record is needed to validate this hypothesis and to fully characterize the long-term STLR dynamics.

The in-situ STLR estimated with  $T_{\max}$  has a seasonal trend. The steepest STLR are reported during the warm and dry season (summer), and the shallowest STLR during the coldest and rainy season (winter). These trends have been reported elsewhere in other mountainous regions (Blandford *et al.*, 2008; Rolland, 2003). On the other hand, the in-situ STLR estimated with  $T_{\min}$  is shallower during the dry season and steeper during the coldest and rainy season; this has also been reported elsewhere (Pepin, 2001; Pepin and Losleben, 2002). Note also

that STLR values estimated with DMC and DGA  $T_{\min}$  do not follow a clear seasonal pattern, as has also been shown for the city of Santiago by Muñoz (2005), who used temperature records from two meteorological stations at 480 and 1,100 m ASL to analyse the STLR between 5:00–7:00 LST, right before dawn when minimum temperatures occur.

To further describe the diurnal and seasonal STLR cycles, a thermoisopleth diagram with weekly STLR averages and  $R^2$  values obtained when fitting the linear regression as a function of the time of the day, are shown in Figure 4 for both WSN and DMC data sets. There is a clear anti-correlation between STLR (Figure 4a,b) and  $R^2$  (Figure 4c,d) due to the fact that gentle STLR are associated with lower  $R^2$ , indicating the likely influence of the inversion layer. The existence of the inversion not only reduces the STLR but also weakens the linear correlation between SAT and altitude. If the inversion is absent, the linear fitting is more robust and the decay of temperature with altitude becomes more marked. Overall, in-situ STLR changes with season, with the largest difference in the monthly average occurring between June (winter) and September (spring) (Table 2). The gentle STLR in late night and morning during spring, summer and fall observed in Figure 4a is consistent with a higher prevalence of temperature inversion that, when present, extends up to about 1,200 m ASL thus encompassing a significant portion of the WSN stations. At the same hours but during winter the STLR is much steeper. Moreover, the in-situ STLR tend to be constant throughout the day during winter, with mean values ranging between  $-5.0$  and  $-4.5^{\circ}\text{C}/\text{km}$  and the lowest  $SD$  of the year ranging between 0.3 and  $0.6^{\circ}\text{C}/\text{km}$  (Table 2). This may seem contradictory with the more intense and prevalent



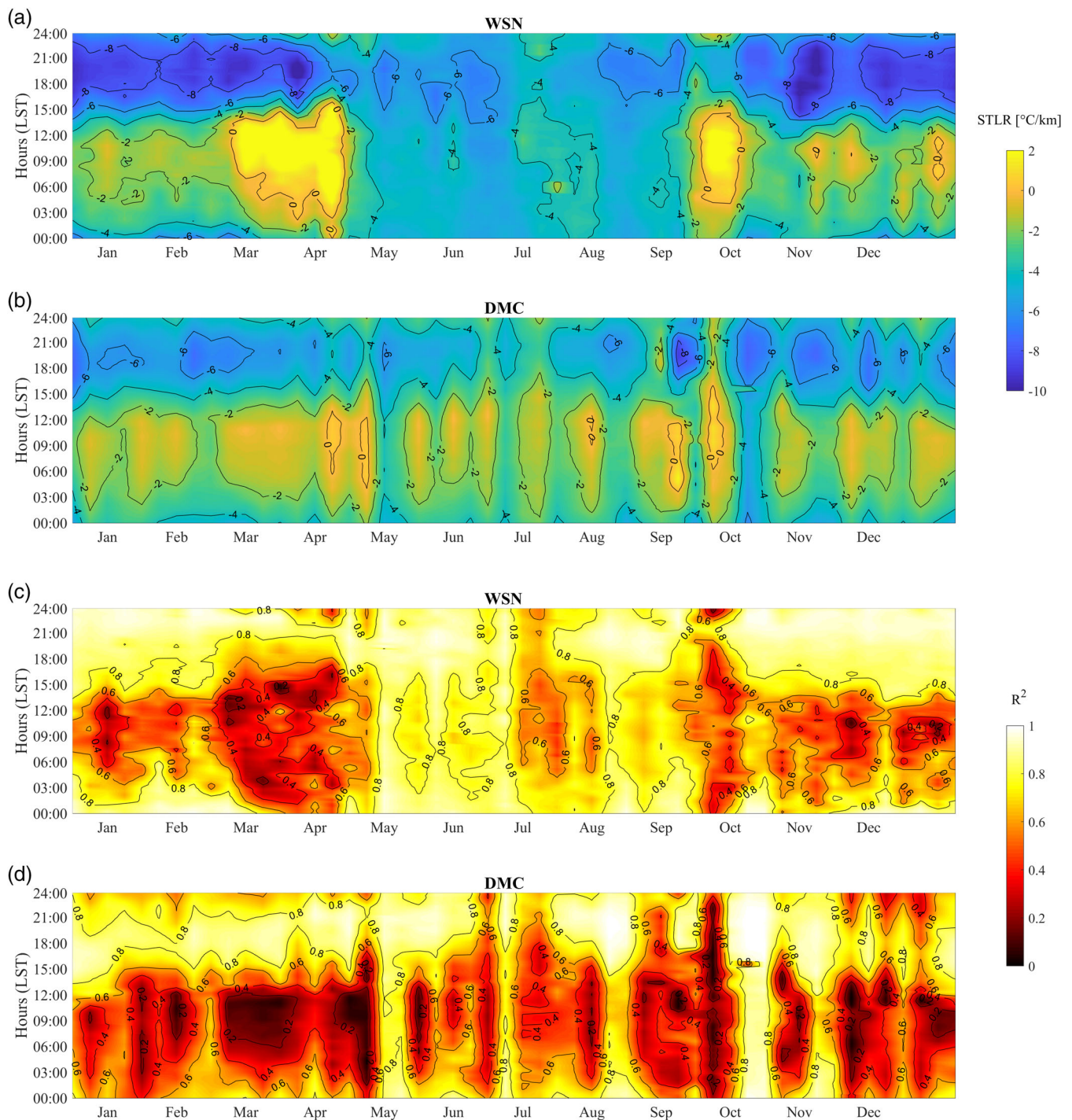


**FIGURE 4** Thermoisopleth diagram showing seasonal variation of the hourly STLR values ( $^{\circ}\text{C}/\text{km}$ ) estimated with the WSN (a) and DMC data sets (b), and the corresponding  $R^2$  coefficients of the linear regression used for their calculations (c and d). Time is shown in local standard time (LST) on a weekly basis [Colour figure can be viewed at [wileyonlinelibrary.com](http://wileyonlinelibrary.com)]

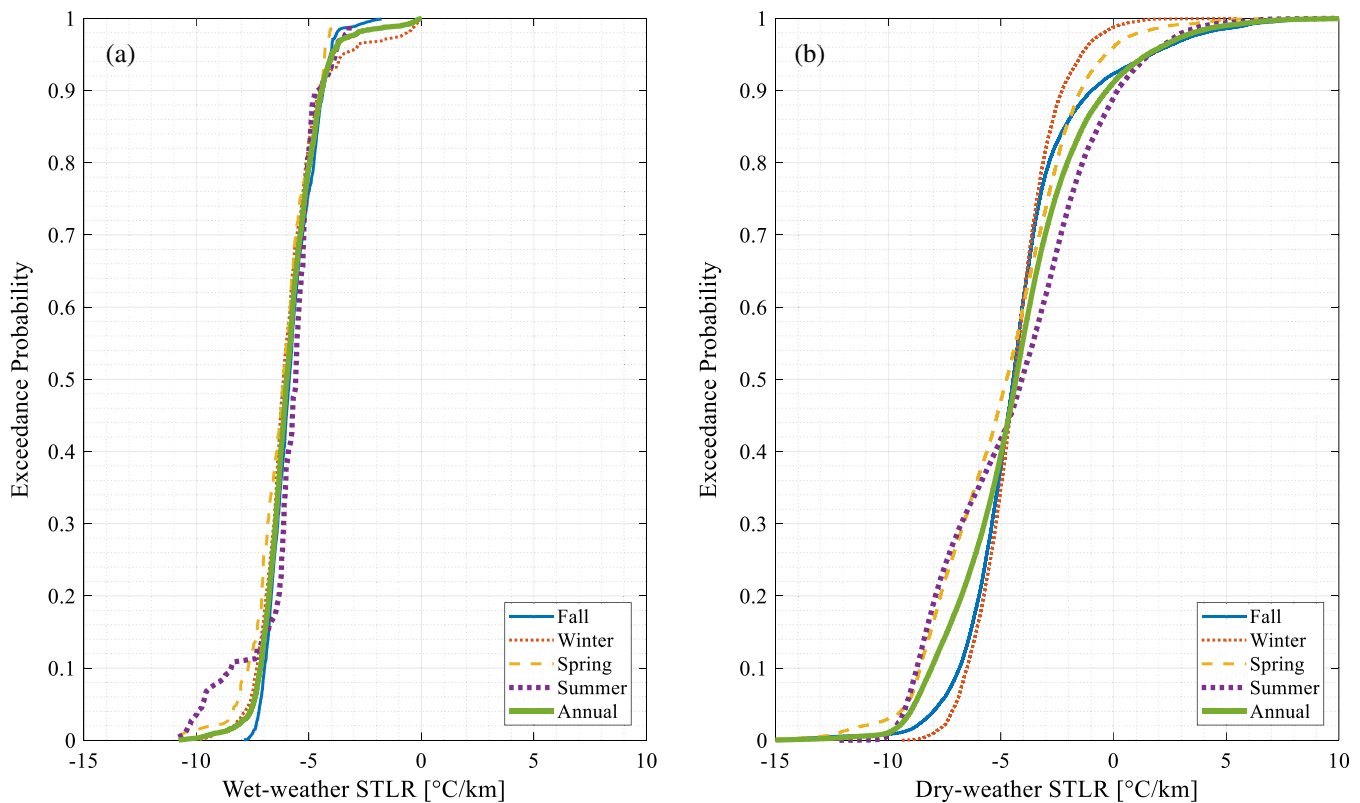
inversions during the cold season of the year (Muñoz and Undurraga, 2010). Nonetheless, the inversions are much shallower during winter night time, with their top below 1,000 m ASL, so they do not reach the vertical range of WSN (see the thermoisopleth diagram built with the DMC station without the highest station available in the

Supporting Information). On the other hand, the largest variability of STLR is observed during late summer (March, Table 2).

STLR values estimated with the DMC data set (Figure 4b) show similar daily trends as the in-situ values STLR values, although there is less variation along the

**TABLE 2** Maximum (max), minimum (min), average (avg) and *SD* of hourly STLR for WSN and DMC data sets (obtained from Figure 4)

Hourly STLR (°C/km)	Jan	Feb	Mar	Apr	My	Jun	Jul	Aug	Sept	Oct	Nov	Dec
WSN-max	-1.6	-1.2	1.1	0.1	-4.3	-4.6	-3.9	-4.0	0.1	-1.7	-1.5	-0.9
WSN-min	-8.7	-8.3	-8.4	-7.3	-6.0	-5.7	-5.5	-5.8	-6.0	-8.4	-8.3	-8.7
WSN-avg	-4.9	-4.4	-3.2	-2.9	-4.8	-5.0	-4.5	-4.6	-2.5	-4.9	-4.8	-4.5
WSN- <i>SD</i>	2.6	2.6	3.4	2.5	0.6	0.3	0.5	0.6	2.0	2.4	2.5	2.9
DMC-max	-1.1	-1.4	-1.1	-0.6	-1.8	-1.4	-1.4	-1.5	-1.4	-2.3	-1.9	-1.6
DMC-min	-6.0	-6.2	-6.1	-5.5	-5.6	-4.7	-4.8	-4.5	-4.9	-6.5	-6.3	-6.2
DMC-avg	-3.3	-3.4	-3.3	-2.7	-3.2	-2.7	-2.7	-2.8	-2.8	-4.1	-3.9	-3.7
DMC- <i>SD</i>	1.7	1.7	1.7	1.7	1.3	1.1	1.1	1.0	1.1	1.4	1.5	1.6

**FIGURE 5** Seasonal and annual exceedance curves of the in-situ STLR (°C/km) for wet-weather (a) and dry-weather (b) conditions calculated with the WSN data set [Colour figure can be viewed at [wileyonlinelibrary.com](http://wileyonlinelibrary.com)]

day. In fact, this variability tends to be more constant throughout the year (Table 2), with monthly *SDs* ranging between 1.0 and 1.7°C/km, as compared with the wider range of values obtained from the WSN data set (between 0.3 and 3.4°C/km). Overall, average STLR values estimated with DMC data set are gentler than the in-situ values for 11 out of 12 months, especially during the wet and cold season between May and August (Table 2). Such differences are due to the altitude range of the meteorological stations in relation to the inversion layer: WSN stations are sometimes located above the inversion while

the low lying DMC stations are mostly embedded in the inversion.

#### 4.2 | Seasonal variation of the in-situ STLR during wet- and dry-weather conditions

Figure 5 presents the exceedance curves of the in-situ STLR values calculated for the different seasons, as well as for the entire year (the annual curve). Figure 5a shows

**TABLE 3** Average, median and *SD* of the WSN STLR values for wet-weather, dry-weather and all-weather conditions (obtained from Figure 5)

Statistic ( $^{\circ}\text{C}/\text{km}$ )	Fall	Winter	Spring	Summer	Annual
Average wet-weather	-5.8	-5.9	-6.2	-5.9	-5.9
Average dry-weather	-4.1	-4.4	-4.9	-4.2	-4.4
Average all-weather	-4.2	-4.5	-5.0	-4.3	-4.5
Median wet-weather	-5.9	-6.1	-6.1	-5.6	-6
Median dry-weather	-4.5	-4.4	-4.8	-4.1	-4.4
Median all-weather	-4.6	-4.5	-4.8	-4.1	-4.6
<i>SD</i> wet-weather	1.0	1.4	1.3	1.5	1.3
<i>SD</i> dry-weather	2.8	1.7	3.0	3.5	2.9
<i>SD</i> all-weather	2.8	1.7	2.9	3.4	2.4

the exceedance curves obtained using in-situ STLR values during the occurrence of precipitation events, while the curves in Figure 5b are built using in-situ STLR values obtained during dry-weather conditions. The mean, median and *SD* of this figure are presented in Table 3. A precipitation event is defined to have a volume larger than 1 mm, while 14 hr is used as the minimum inter-arrival time to separate independent events, as suggested by Zegpi and Fernandez (2010) in the study area.

Interestingly, the exceedance probabilities associated with the in-situ STLR values for wet-weather conditions are very similar, for all the seasons, especially for probabilities between 0.11 and 0.92, associated with values between  $-7.5$  and  $-4.2^{\circ}\text{C}/\text{km}$ . The average in-situ STLR values range between  $-5.8$  and  $-6.2^{\circ}\text{C}/\text{km}$  for all the seasons, while the median values range between  $-5.6$  and  $-6.1^{\circ}\text{C}/\text{km}$  (Table 3). These STLR values are similar to those reported elsewhere under rainy conditions (Blandford *et al.*, 2008; González and Garreaud, 2019), reflecting that during precipitation events the air is close to saturation and there is enough vertical mixing as to approach the moist adiabatic lapse rate in the lower troposphere. On the other hand, the tails of the curves differ among them (Figure 5a), although more similar shapes are observed for the fall, winter and annual curves. Because only a few precipitation events were recorded during spring and summer, we expect the resulting exceedance curves to not be conclusive for these seasons. Finally, note that thermal inversions (i.e.,  $\text{STLR} > 0^{\circ}\text{C}/\text{km}$ , right tail) are not reported under wet-weather conditions.

For the dry-weather conditions, non-systematic but relevant differences in the exceedance curves for the in-situ STLR values among the seasons are observed (Figure 5b). For example, summer presents the lowest values between probabilities 0.04 and 0.33 and the highest between 0.47 and 0.95, and the winter present the highest values until 0.47 and then the lowest from 0.65. Nonetheless, around probability 0.5, values tend to

be similar regardless the season, with the medians ranging from  $-4.1^{\circ}\text{C}/\text{km}$  (summer) to  $-4.8^{\circ}\text{C}/\text{km}$  (spring) (Table 3), and an annual median of  $-4.4^{\circ}\text{C}/\text{km}$ . Furthermore, Figure 4b shows that thermal inversion during dry-weather conditions occurs in all seasons, although such occurrence varies from 1% of the time during winter up to 10% during summer.

As expected, the *SD* for wet-weather is lower than for dry-weather conditions, ranging between  $1.0$  and  $1.5^{\circ}\text{C}/\text{km}$  and  $1.7$  and  $3.5^{\circ}\text{C}/\text{km}$ , respectively (Table 3). Finally, and because dry-weather conditions are predominant, the exceedance curves for each season obtained after combining wet- and dry-weather data are very similar to the corresponding dry-weather curves (not shown). Hence, the statistics of the curves are almost the same, with differences in the average, median and *SD* being  $0.1^{\circ}\text{C}/\text{km}$  or smaller (Table 3).

The overall weaker negative STLR values calculated for dry-weather conditions tend to be gentler than the dry-adiabatic lapse rate of  $(-9.8^{\circ}\text{C}/\text{km})$ . As said before, these values are explained by the occurrence of thermal inversion during dry-weather conditions, together with the fact that less negative STLR values and low associated  $R^2$  coefficients are obtained under these circumstances. Figure 6 illustrate this issue by comparing the boxplots of the  $R^2$  values for wet- and dry-weather conditions (Figure 6a,b) obtained using WSN and DMC data. Furthermore, Figure 6c,d illustrate two linear regressions fitted using the WSN data for wet- and dry-weather conditions, whose slopes equal the median in-situ STLR for each case ( $-6.0$  and  $-4.3^{\circ}\text{C}/\text{km}$ , respectively).  $R^2$  coefficients for wet-weather conditions are much higher than for dry-weather conditions, regardless of the data set. Because of (a) the poor estimation of STLR values for dry-weather conditions when thermal inversion occurs in the study zone, and (b) the good fitting of linear regression when rain takes place and flash flood events may occur, we now study in detail the behaviour of the STLR and  $H_0$  under wet-weather conditions.

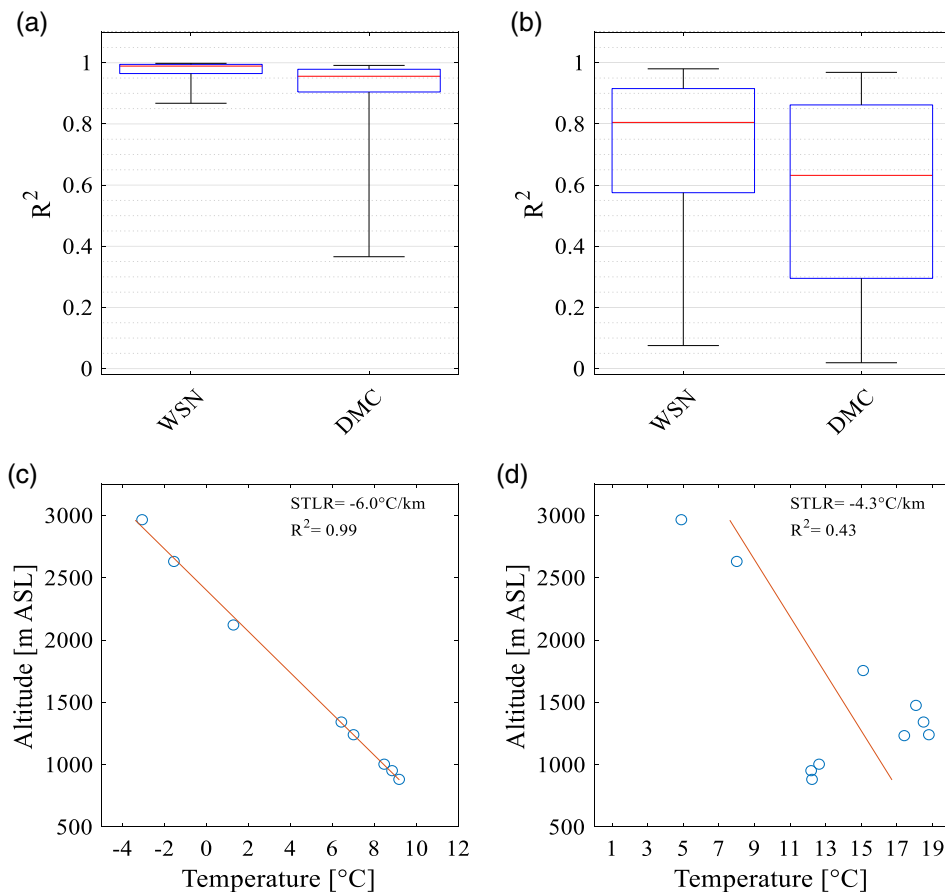


**FIGURE 6**  $R^2$  coefficients of the linear regression fitted under (a) wet-weather conditions and (b) dry-weather condition using the WSN and DMC data sets panels (c) and (d) show representative linear fittings for both wet- and dry conditions using the WSN data set. In each boxplot, the central line indicates the median and the edges of the box indicate the 25th and 75th percentile, and the whiskers correspond to the minimum and maximum values without considering outliers [Colour figure can be viewed at [wileyonlinelibrary.com](http://wileyonlinelibrary.com)]

### 4.3 | Behaviour of STLR and H0 during wet-weather conditions

The characterization of the STLR and H0 during precipitation events in the study area is relevant because warmer temperatures may lead to floods and flash floods by increasing the direct runoff area. Garreaud (2013) identified warm winter storms in central Chile as those in which the air temperature in downtown Santiago (Quinta Normal station) exceeds  $10.5^\circ\text{C}$  during the rain period (i.e.,  $\sim 30\%$  of the winter storms). Most of these storms often feature an atmospheric river impinging against the Andes Mountains (Valenzuela and Garreaud, 2019), thus increasing the likelihood of extreme hydrometeorological events with detrimental impact downstream (Garreaud and Rutllant, 1997; Garreaud, 2013).

Figure 7 shows boxplots of the in-situ STLR and H0 for warm and cold storm events using the Garreaud (2013) criterion. As expected, most of the H0 distribution during warm events is higher than during cold events (Figure 7b). For instance, the mean H0 goes from 2,120 m ASL for cold events to 2,775 m ASL for warm events. This  $\sim 600$  m difference implies a  $\sim 50\%$  increase in the contributing area of the basin between warm and cold storms. The STLR distributions (Figure 7a) also differ between warm and cold

events, with a difference in mean values ( $-5.6$  and  $-5.9^\circ/\text{km}$ , respectively) statistically significant at the 1% level of significance, which means rising H0  $\sim 90$ – $120$  m more. Thus, higher H0s during warm storms are explained not only by warmer temperatures, but also gentler STLR (to a lesser extent).

Although STLR varies temporally and spatially, several hydrological models such as the Hydrologic Modelling System (HEC-HMS, Scharffenberg and Fleming, 2010) use a constant STLR value to simulate rainfall-runoff and snow processes. Indeed, constant STLR values have been used in several studies in the study area and for the central Andes in general. For example, Meza *et al.* (2012) used a STLR of  $-6.5^\circ\text{C}/\text{km}$  to evaluate the potential impact of climate change on the hydro-climatological regime of the Maipo basin. Moreover, Cavieres *et al.* (2000) used a STLR of  $-6.1^\circ\text{C}/\text{km}$  to characterize the altitudinal vegetation belts in the high-Andes of central Chile. Thus, it becomes relevant to explore the implications of assuming a constant STLR value during wet-weather conditions using the continuous in-situ information available from our study.

Figure 8a presents boxplots for the absolute error in the estimation of H0 obtained by extrapolating the temperatures at station Quinta Normal using nine different

**FIGURE 7** Boxplot of in-situ STLR ( $^{\circ}\text{C}/\text{km}$ ) (a) and  $0^{\circ}\text{C}$  isotherm altitude (b) calculated for wet-weather conditions when the temperature in Quinta Normal DMC Station is over  $10.5^{\circ}\text{C}$  (warm events) and cold events. Number above each box indicate the number of storms in each group and total duration involved [Colour figure can be viewed at [wileyonlinelibrary.com](http://wileyonlinelibrary.com)]

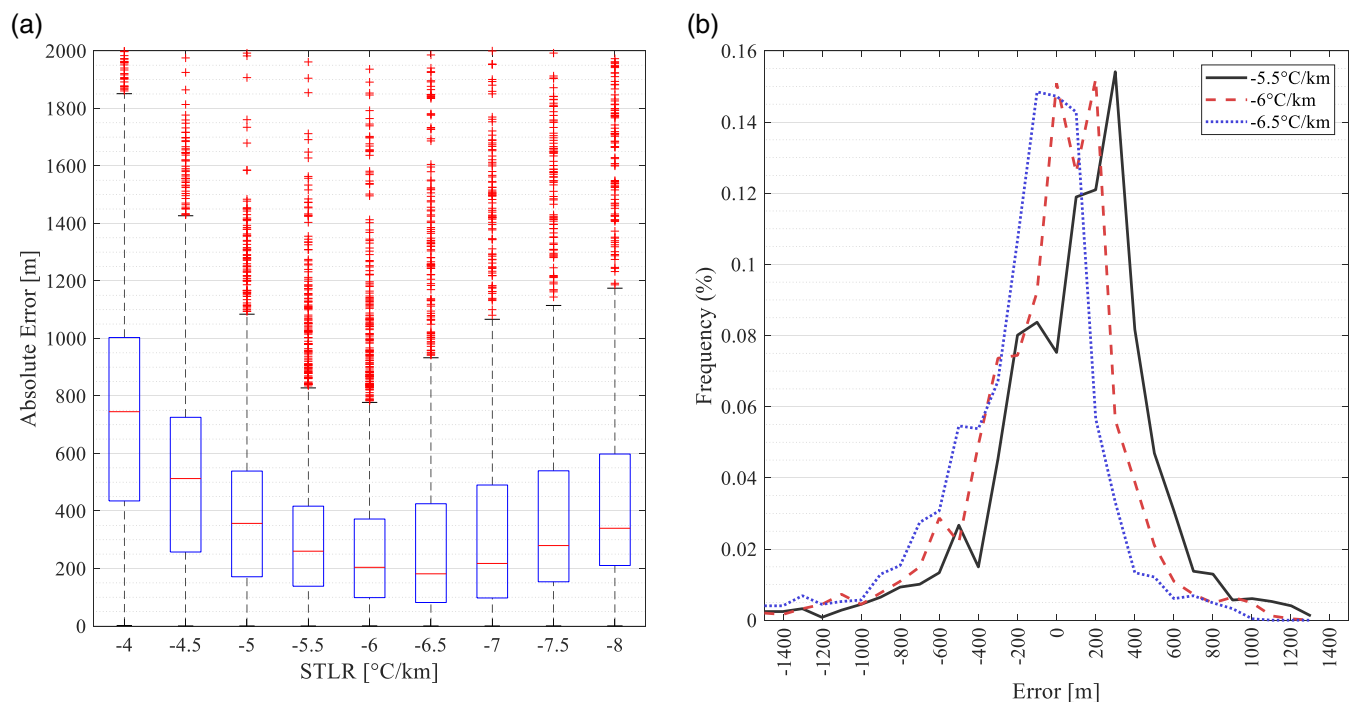
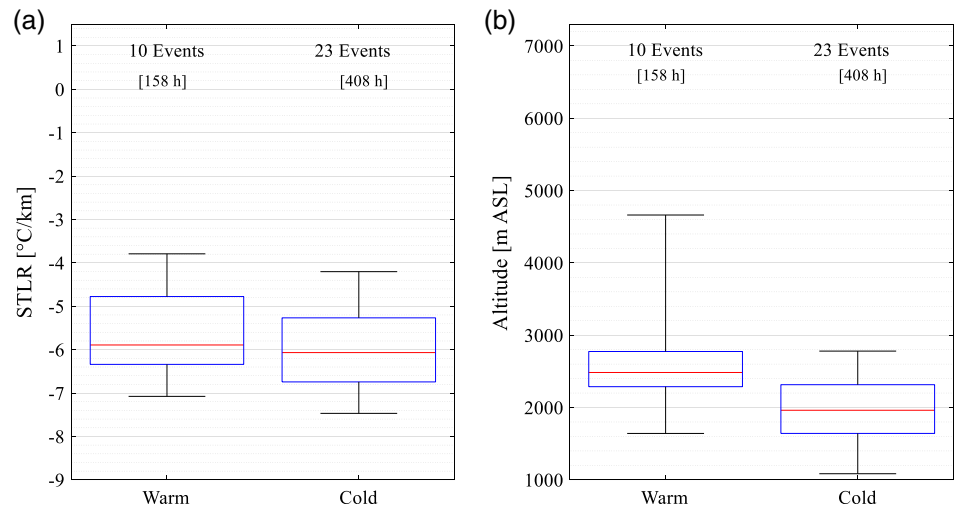


**FIGURE 8** (a) Boxplot of absolute errors when estimating the in-situ  $0^{\circ}\text{C}$  isotherm during wetweather condition using an extrapolation of temperatures from Quinta Normal and different constant values of STLR ( $^{\circ}\text{C}/\text{km}$ ). (b) Line histogram chart of the errors associated with constant STLR values of  $-5.5$ ,  $-6.0$  and  $-6.5^{\circ}\text{C}/\text{km}$ , using a bin size of 100 m [Colour figure can be viewed at [wileyonlinelibrary.com](http://wileyonlinelibrary.com)]

constant STLR values, relative to the in-situ value obtained from the WSN. The smallest errors are obtained with constant STLR values of  $-5.5$ ,  $-6.0$  and  $-6.5^{\circ}\text{C}/\text{km}$ . The medians of these errors are 260, 204 and 181 m, respectively. Moreover, 50% or more of the errors associated with these STLR values exceed 200 m, while 20% or more of the errors exceed 500 m. Figure 8b shows the line histogram chart of relative frequency of the errors using constant STLR values of  $-5.5$ ,  $-6.0$  and  $-6.5^{\circ}\text{C}/\text{km}$ . Positive and negative errors quite centred around zero are

obtained for these three STLR values, with a slight bias towards overestimation when using  $-5.5^{\circ}\text{C}/\text{km}$ , and underestimation when using  $-6.5^{\circ}\text{C}/\text{km}$ . Overall, under wet-weather conditions, extrapolating temperatures of Quinta Normal station using an STLR value of  $-6.0^{\circ}\text{C}/\text{km}$  allow the best estimation of  $H_0$ . Nonetheless, errors up to  $\pm 400$  m are not uncommon during some precipitation events, which may have important consequences when estimating direct surface runoff. This will be further analysed in Section 5.

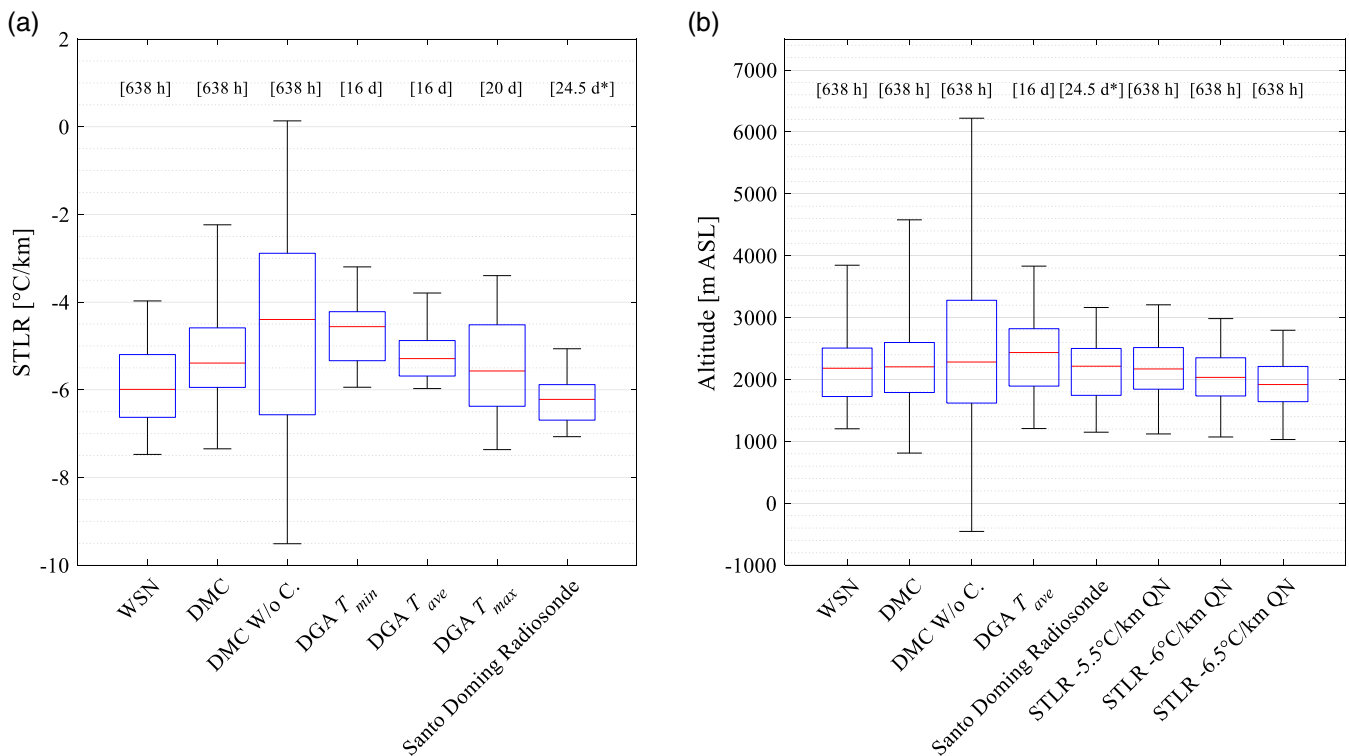
#### 4.4 | Estimation of STLR, FTLR, and H0 during Wet-Weather conditions using different data sets

Figure 9a presents the boxplots for the STLR values calculated during wet conditions obtained from the WSN data set, the DMC and DGA data sets, as well as for the FTLR estimated using the Santo Domingo radiosonde data. To further study the implications of having a temperature gauge located at a high elevation, DMC boxplots calculated with and without using the Colorado gauge (the highest DMC gauge located at 2,750 m ASL) are shown. Furthermore, because DGA gauges only record the minimum and maximum daily temperatures, we consider three boxplots calculated from the  $T_{\min}$  and  $T_{\max}$  measured in these gauges as well as  $T_{\text{ave}}$ , referred to as the DGA  $T_{\min}$ , DGA  $T_{\text{ave}}$ , and DGA  $T_{\max}$ . On the other hand, Figure 9b compares five estimations of H0 associated with different data sets and three extrapolations of temperatures using the Quinta Normal gauge and constant STLR values of  $-5.5$ ,  $-6.0$  and  $-6.5^\circ\text{C}/\text{km}$ .

Similar STLR values are obtained from the DMC and WSN data sets (Figure 9a), although the interquartile range for the former is smaller and the median is higher. However, the boxes for the corresponding H0 (Figure 9b)

are almost identical, with similar interquartile ranges and medians. If the Colorado gauge is not considered, much larger interquartile and minimum-maximum ranges are observed for STLR and H0. This is explained by the large influence of Colorado gauge when fitting the linear regression. Moreover, the corresponding medians for these variables increase up to  $-4.3^\circ\text{C}/\text{km}$  and 2,282 m ASL, respectively. Hence, using temperature gauges at high elevations is key for a proper estimation of STLR and H0.

The boxplots of STLR obtained with the DGA data set (Figure 9a) clearly differ depending on whether  $T_{\min}$ ,  $T_{\text{ave}}$  or  $T_{\max}$  is used for the estimation. Nonetheless, the three medians are gentler than the in-situ median STLR. The STLR estimated with  $T_{\text{ave}}$  has the smaller interquartile range, while DGA  $T_{\max}$  has the largest range. On the other hand, the  $0^\circ\text{C}$  isotherm elevations estimated with the DGA  $T_{\text{ave}}$  (Figure 9b) tend to be similar to the ones obtained with the WSN data set, although there is a tendency to overestimate the median value (2,436 m ASL vs. 2,174 m ASL). Despite the existence of a high station at 2,475 m ASL in the DGA network, the range and distribution of STLR and H0 estimations still differs significantly from those observed in-situ. This fact illustrates the relevance of the time step used in SAT monitoring, as the DGA data are just daily.



**FIGURE 9** Boxplots comparing STLR values ( $^\circ\text{C}/\text{km}$ ) (a), and  $0^\circ\text{C}$  isotherm height (b), during wet-weather conditions calculated with different data sets. Values above the boxes correspond to the number of hours or days involved in the calculation (d and d\* denote one and two measurements per day, respectively) [Colour figure can be viewed at [wileyonlinelibrary.com](http://wileyonlinelibrary.com)]

The ranges of H0 values obtained from the extrapolation of Quinta Normal temperatures using constant lapse rates are smaller than those estimated with the WSN data set (Figure 9b). Notably, the median values obtained using a constant STLR of  $-6.0^{\circ}\text{C}/\text{km}$  and the WSN data differ by less than 4 m; nevertheless, the differences for the 25th and the 75th percentiles are larger (121 and 45 m, respectively).

Finally, FTLR values calculated with the sounding data are the least spread among all the datasets (boxplot height in Figure 9a), while a median value of  $-6.2^{\circ}\text{C}/\text{km}$  similar to the in-situ value is obtained. Moreover, the range of H0 estimated with the sounding data is also very similar to the values estimated with WSN (Figure 9b) with difference in the median of 41 m, while for the 25th and 75th percentile the differences are 22 and 60 m, respectively. The Santo Domingo radiosonde station is at the coast where the lower troposphere often (more than 70% of the time) features a marine boundary layer capped by a temperature inversion with its base at about 500 m ASL, more or less coincident with the floor of the Santiago basin (Garreaud and Rutllant, 2004). This configuration, however, disappears during rainy episodes as large-scale subsidence changes to ascending motion in connection with an approaching front. Under these conditions, the mixing boundary layer thermal inversions is replaced by a well-mixed, near saturated layer, thus explaining the excellent agreement between the coastal FTLR and the Andean STLR, as well as between H0 derived from the sounding and the surface data. Also note that the sounding system drifts eastward during its ascent getting closer to and eventually crossing the Andes range. While the sounding-base lapse rate is slightly stronger than the lapse rate derived from WSN, their distribution largely overlap and we cannot conclude they differ significantly. On the other hand, the lapse rates from DGA are gentler than other estimate because as commented in Section 4.1. Despite these differences, the mean values of H0 from different sources are quite similar and H0 derived from the sounding results the lowest. Such compensation suggests the existence of a horizontal temperature gradient

from the coast to the Andean foothills, but addressing such issue is beyond the scope of this work.

## 5 | IMPLICATIONS ON THE HYDROLOGICAL RESPONSE AND ITS MODELLING

To understand the impact of the STLR values on the hydrological response and its modelling, we assess the effect of using various STLR estimations on the total amount of liquid precipitation that falls in different storms over the Quebrada de Ramón basin. Calculation of runoff is beyond the scope of this paper as it requires knowing the precipitation distribution with height and the infiltration rates for all the events. Hence, we provide a rough estimate by considering the total liquid precipitation over the contributing area. The total liquid precipitation is calculated as the integral of the point precipitation over the area ( $P(h)dA$ ) in which rainfall occurs.  $P(h)$  is the point precipitation throughout the watershed that is computed using a linear precipitation gradient, similar to the example developed for the study catchment by Garreaud (2013). This gradient is obtained individually for each storm using the total precipitation recorded at two WSN rain gauges: Reforestación at 945 m ASL and Provincia Bajo at 2,117 m ASL (Table 1). Although the true precipitation distribution with the height is complex, assuming a linear model gives an idea of the impact that different STLR estimates have over runoff estimation.

We apply this methodology to four rainfall events during 2017 (Table 4) and assume that only liquid precipitation fell on the gauges. This assumption is supported by the temperature records during these events, which ensure liquid precipitation occurring at the elevations where the rain gauges are located. The magnitude of these events covers a wide range of values typical of the area (1.6–45 mm). The direct runoff contributing area at a given time corresponds to the area of the basin below H0, and is obtained from the available watershed hypsometric curve (Pérez, 2011). The total amount of precipitated water is

**TABLE 4** Percentage of error in precipitated water calculated using different data sets for four precipitation events of 2017

Event date	Magnitude (mm)	Duration (h)	DMC	DGA	DGA	DGA	SD radiosonde	QN	QN	QN
				$T_{\max}$	$T_{\text{avg}}$	$T_{\min}$		$-5.5^{\circ}\text{C}/\text{km}$	$-6.0^{\circ}\text{C}/\text{km}$	$-6.5^{\circ}\text{C}/\text{km}$
May 8, 2017	11.6	6.1	7.7%	26.4%	26.4%	26.4%	-1.9%	-1.4%	-11.6%	-21.5%
May 11–12, 2017	44.9	23.6	11.7%	35.2%	31.4%	-6.8%	13.1%	19.4%	8.5%	-2.6%
May 26, 2017	1.6	7.1	-8.8%	45.0%	32.5%	-85.2%	-0.7%	-38.5%	-49.0%	-58.4%
June 26–27, 2017	6.9	30.5	7.8%	39.4%	22.7%	-62.9%	-9.9%	0.1%	-11.1%	-21.5%

Note: The precipitation estimated using the WSN data set is the reference for the assessment.

finally obtained by the temporal accumulation of the spatial integral of precipitation. Because the time resolution of the precipitation records is also 10 min in the WSN, direct runoff contributing areas can be estimated with this resolution using the WSN and the DMC data sets. On the other hand, the coarse time resolutions of the soundings and the DGA data sets allow for one or at most two direct runoff contributing area estimations during each event, depending on its duration.

Table 4 presents the percentage of error of the total volume of precipitated water using as reference the total amount estimated with the in-situ  $H_0$  obtained from the WSN. The lowest errors from ground measurements are obtained when using the DMC data set; this is expected as its time resolution and the existence of a station at high elevation (Colorado) allow tracking  $H_0$  captured by the WSN gauges, as shown in Figure 9b. The highest overestimation is produced when using the lapse rates obtained from the DGA  $T_{\max}$  data set, with errors ranging between 26 and 45% for the different events. In this case,  $H_0$  and the contributing area are overestimated because  $T_{\max}$  is larger than the temperatures during the event. As expected, the opposite phenomenon occurs when using the DGA  $T_{\min}$  data set, despite the gentler STLR. In this case, rainfall volumes are underestimated for three of the events, with an error of  $-85\%$  being the largest one. Using the DGA  $T_{\text{avg}}$  data set produces overestimations in the volume between 26 and 32%.

The sounding data leads to relatively small errors, with underestimations up to  $-10\%$  for three events and an overestimation of 13% for the remaining event; this is because of the good agreement between the height of the  $0^\circ\text{C}$  isotherm estimated with the sounding data and the in-situ  $H_0$ , as explained in Section 4.4. Finally, for three of the four events, the error associated with the extrapolation from Quinta Normal temperature using a constant STLR of  $-6.5^\circ\text{C}/\text{km}$  is smaller than when using  $-6.0$  and  $-5.5^\circ\text{C}/\text{km}$ . However, for the May 26th event, the three STLR values produce large underestimations, with errors larger than  $-38\%$ . The highest underestimation in this case is obtained when using a  $-6.5^\circ\text{C}/\text{km}$  STLR. Overall, these results illustrate the relevance of using time-variant  $H_0$  measured in-situ when modelling the hydrologic response in high-relief environments, where liquid and solid precipitation can occur. Approximations based on nearby information or fixed STLR may lead to errors that can significantly affect the estimation of flow discharges and runoff volume.

## 6 | CONCLUSIONS

This paper has studied empirically the daily and seasonal variability of the surface temperature lapse rate (STLR)

and the  $0^\circ\text{C}$  isotherm height ( $H_0$ ) in the western slope of the sub-tropical Andes, a region prone to flash floods due to its steep, bare slopes and the occasional occurrence of rainfall events with warm temperatures. A 2-year record of temperatures registered every 10 min in 16 gauges in the Quebrada de Ramon basin (the foothills of Santiago, the Chilean Capital) at elevations between 878 and 2,962 m ASL, was used for this purpose. Results were compared against those obtained using nearby stations with long records and operated by the weather and water agencies on a routine basis. The hydrological implications of the different estimations of  $H_0$  were studied by comparing total amounts of liquid precipitation in the basin for four precipitation events during 2017. The following are the main conclusions of the study:

- Significant intra- and inter-day variations of the in-situ STLR are observed. Large differences are detected among seasons for different times of the day, with the gentler STLR occurring during late night and early morning (around 9:00 LST) and the steepest ones later during the day.
- In-situ STLR values differ among wet- and dry-weather conditions. During wet-weather conditions, STLR values are more similar regardless of the season, the average ranges between  $-5.8$  and  $6.2^\circ\text{C}/\text{km}$ , with annual average of  $-5.9^\circ\text{C}/\text{km}$ . For dry-weather conditions, STLR values are more variable, the seasonal average range between  $-4.1$  to  $-4.9^\circ\text{C}/\text{km}$  and the annual average is  $-4.4^\circ\text{C}/\text{km}$ . Also, STLR under dry-weather conditions are poorly obtained from linear regressions due to the occurrence of thermal inversions.
- STLR values during warm storm events (i.e., events with a temperature of  $10.5^\circ\text{C}$  measured in Santiago) are slightly less pronounced (mean of  $-5.6^\circ\text{C}/\text{km}$ ) compared with the observations during cold events (mean of  $-5.9^\circ\text{C}/\text{km}$ ). Thus, the effect of higher temperatures in the rising of  $H_0$  during warm events is to some extent enhanced by gentler STLR. Differences of  $\sim 600$  m in the median  $H_0$  values imply a 50% increase in the contributing area of the basin when warm events occur.
- The free-air temperature lapse rate estimated (FTLR) and  $H_0$  using regional atmospheric sounding are in a good agreement with the in-situ STLR and the  $H_0$  derived from the WSN data set. Hence, good estimations of the amount of precipitated water for four different storm events are obtained atmospheric sounding data.
- Despite the existence of a temperature station at a high elevation, daily minimum, maximum and average temperature data collected by DGA do not allow the adequate estimation of the range and distribution of in-situ STLR and  $H_0$ . This fact illustrates the relevance of using fine time steps in temperature monitoring.





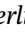
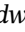

- Overall, if a single STLR constant value is to be used for hydrological modelling in the study area during wet-weather conditions, the best option is between  $-5.5$  and  $-6.5^{\circ}\text{C}/\text{km}$ , with  $-6.0^{\circ}\text{C}/\text{km}$  giving slightly better results. These values are similar to the annual in-situ STLR average for wet-weather conditions. However, these values are not representative of the in-situ STLR during warm precipitation events, as an average of  $-5.6^{\circ}\text{C}/\text{km}$  was found for these events. This issue is critical as warm events typically cause flash floods in the area.

This study is one of the few ones reporting the hourly, daily and seasonal dynamics of the STLR and  $0^{\circ}\text{C}$  isotherm high in the Andes Mountains. Nonetheless, caution must be taken when using our results, as they were obtained from data collected for only 2 years in a single small catchment. Future research should consider replicating the monitoring campaign and analysis in other latitudes along the Andes. Future monitoring campaigns must also consider more stations at higher elevations and time periods longer than 2 years, given the variability observed in our study, and the potential occurrence of the ENSO effect. Furthermore, we encourage an additional focus on the spatial variability of the STLR, as its dynamics may be different even within nearby basins.

## ACKNOWLEDGEMENTS

This study was funded by projects FONDAP 15110017 and Fondecyt grant 1161439. We also acknowledge the support from Instituto Nacional de Hidráulica (CHILE) and project FONDEF IT13i20015 to implement the wireless sensor network. María Ibáñez acknowledges the scholarship from Fundación San Carlos del Maipo, while Jorge Gironás thanks the support from FONDAP 15110020. René Garreaud is supported by FONDAP 15110009. Comments and suggestions from Dr Héctor Jorquera and an anonymous reviewer are appreciated. Public data used are available from <http://www.meteochile.gob.cl/PortalDMC-web/index.xhtml> (DMC data), <http://snia.dga.cl/BNAConsultas/reportes> (DGA data) and <http://weather.uwyo.edu/upperair/sounding.html> (Sounding data). The WSN data are available from Ibáñez *et al.* (2019).

## ORCID

María Ibáñez  <https://orcid.org/0000-0001-7454-3057>  
 Jorge Gironás  <https://orcid.org/0000-0002-6933-2658>  
 Christian Oberli  <https://orcid.org/0000-0003-3068-096X>  
 Cristián Chadwick  <https://orcid.org/0000-0002-9209-4352>  
 René D. Garreaud  <https://orcid.org/0000-0002-7875-2443>

## REFERENCES

- Blandford, T., Humes, K., Harshburger, B., Moore, B., Walden, V. and Ye, H. (2008) Seasonal and synoptic variations in near-surface air temperature lapse rates in a mountainous basin. *Journal of Applied Meteorology and Climatology*, 47(1), 249–261. <https://doi.org/10.1175/2007JAMC1565.1>.
- Bolstad, P., Swift, L., Collins, F. and Régnière, J. (1998) Measured and predicted air temperatures at basin to regional scales in the southern Appalachian Mountains. *Agricultural and Forest Meteorology*, 91(3–4), 161–176. [https://doi.org/10.1016/S0168-1923\(98\)00076-8](https://doi.org/10.1016/S0168-1923(98)00076-8).
- Brunt, D. (1933) The adiabatic lapse-rate for dry and saturated air. *Quarterly Journal of the Royal Meteorological Society*, 59(252), 351–360. <https://doi.org/10.1002/qj.49705925204>.
- Cannon, A., Neilsen, D. and Taylor, B. (2012) Lapse rate adjustments of gridded surface temperature normals in an area of complex terrain: atmospheric reanalysis versus statistical up-sampling. *Atmosphere-Ocean*, 50(1), 9–16. <https://doi.org/10.1080/07055900.2011.649035>.
- Castro, L., Gironás, J., Escauriáza, C., Barría, P. and Oberli, C. (2019) Meteorological characterization of floods in a mountainous poorly gauged catchment using principal component analysis. *Journal of Hydrologic Engineering*, 24(11), 05019027. [https://doi.org/10.1061/\(ASCE\)HE.1943-5584.0001852](https://doi.org/10.1061/(ASCE)HE.1943-5584.0001852).
- Caviries, L., Peñaloza, A. and Arroyo, M. (2000) Altitudinal vegetation belts in the high-Andes of Central Chile (33 S). *Revista Chilena de Historia Natural*, 7(3), 331–344. <https://doi.org/10.4067/S0716-078X2000000200008>.
- Chae, H., Lee, H., Lee, S., Cheong, Y., Um, G., Mark, B. and Patrick, N. (2012) Local variability in temperature, humidity and radiation in the BaekduDaegan Mountain protected area of Korea. *Journal of Mountain Science*, 9(5), 613–627. <https://doi.org/10.1007/s11629-012-2347-0>.
- Comin, A., Schumacher, V., Justino, F. and Fernández, A. (2018) Impact of different microphysical parameterizations on extreme snowfall events in the southern Andes. *Weather and Climate Extremes*, 21, 65–75. <https://doi.org/10.1016/j.wace.2018.07.001>.
- Córdova, M., Céleri, R., Shellito, C., Orellana-Alvear, J., Abril, A. and Carrillo-Rojas, G. (2016) Near-surface air temperature lapse rate over complex terrain in the southern Ecuadorian Andes: implications for temperature mapping. *Arctic, Antarctic, and Alpine Research*, 48(4), 673–684. <https://doi.org/10.1657/AAAR0015-077>.
- Falvey, M. and Garreaud, R. (2007) Wintertime precipitation episodes in Central Chile: associated meteorological conditions and orographic influences. *Journal of Hydrometeorology*, 8, 171–193. <https://doi.org/10.1175/JHM562.1>.
- Fuenzalida, H., Sanchez, R. and Garreaud, R. (2005) A climatology of cut off lows in the southern hemisphere. *Journal of Geophysical Research*, 110, D1801. <https://doi.org/10.1029/2005JD005934>.
- Garreaud, R. (2013) Warm winter storms in Central Chile. *Journal of Hydrometeorology*, 14(5), 1515–1534. <https://doi.org/10.1175/JHM-D-12-0135.1>.
- Garreaud, R., Alvarez-Garretón, C., Barichivich, J., Pablo Boisier, J., Christie, D., Galleguillos, M., et al. (2017) The 2010–2015 mega drought in Central Chile: impacts on regional hydroclimate

- and vegetation. *Hydrology and Earth System Sciences*, 21, 1–21. <https://doi.org/10.5194/hess-21-1-2017>.
- Garreaud, R. and Rutllant, J. (1997) Precipitación estival en los Andes de Chile central: aspectos climatológicos. *Atmosfera*, 10, 191–211.
- Garreaud, R. and Rutllant, J. (2004) Factores meteorológicos de la contaminación atmosférica en Santiago. In: Morales, R. and Gonzalez, C. (Eds.) *Capítulo 2 en Episodios Críticos de Contaminación Atmosférica en Santiago*. Universidad de Chile: Colección de Química Ambiental. 9–36.
- Garreaud, R., Vuille, M., Compagnucci, R. and Marengo, J. (2009) Present-day south American climate. *PALAEO3 Special Issue (LOTRED South America)*, 281, 180–195. <https://doi.org/10.1016/j.paleo.2007.10.032>.
- González, S. and Garreaud, R. (2019) Spatial variability of near-surface temperature over the coastal mountains in southern Chile (38°S). *Meteorology and Atmospheric Physics*, 131, 89–104. <https://doi.org/10.1007/s00703-017-0555-4>.
- Hamlet, A. and Lettenmaier, D. (2005) Production of temporally consistent gridded precipitation and temperature fields for the continental United States. *Journal of Hydrometeorology*, 6(3), 330–336. <https://doi.org/10.1175/JHM420.1>.
- Hanna, E., Mernild, S., Yde, J. and Villiers, S. (2017) Surface air temperature fluctuations and lapse rates on Olivares gamma glacier, Rio Olivares basin, Central Chile, from a novel meteorological sensor network. *Advances in Meteorology*, 2017, 1–15. <https://doi.org/10.1155/2017/6581537>.
- Ibañez, M., Gironás, J., Oberli, C. 2019. Data underlying “daily and seasonal variation of the surface temperature lapse rate and 0°C isotherm in the central Chilean Andes mountains”. <https://doi.org/10.17605/OSF.IO/E8F6B>
- Immerzeel, W., Petersen, L., Ragettli, S. and Pellicciotti, F. (2014) The importance of observed gradients of air temperature and precipitation for modeling runoff from a glacierized watershed in the Nepalese Himalayas. *Water Resources Research*, 50(3), 2212–2226. <https://doi.org/10.1002/2013WR014506>.
- Instituto Nacional de Estadísticas (INE) 2018. Síntesis de los Resultados Censo. Available at: <https://www.censo2017.cl> [Accessed 2nd July 2019].
- Kattel, D., Yao, T., Yang, K., Tian, L., Yang, G. and Joswiak, D. (2013) Temperature lapse rate in complex mountain terrain on the southern slope of the Central Himalayas. *Theoretical and Applied Climatology*, 113(3–4), 671–682. <https://doi.org/10.1007/s00704-012-0816-6>.
- Kattel, D., Yao, T., Yang, W., Gao, Y. and Tian, L. (2015) Comparison of temperature lapse rates from the northern to the southern slopes of the Himalayas. *International Journal of Climatology*, 35 (15), 4431–4443. <https://doi.org/10.1002/joc.4297>.
- Kattel, D., Yao, T. and Panday, P. (2018) Near-surface air temperature lapse rate in a humid mountainous terrain on the southern slopes of the eastern Himalayas. *Theoretical and Applied Climatology*, 132(3–4), 1129–1141. <https://doi.org/10.1007/s00704-017-2153-2>.
- Kottek, M., Grieser, J., Beck, C., Rudolf, B. and Rubel, F. (2006) World map of the Köppen-Geiger climate classification updated. *Meteorologische Zeitschrift*, 15(3), 259–263. <https://doi.org/10.1007/s00704-012-0816-6>.
- Lara, M. and Sepúlveda, S. (2010) Landslide susceptibility and hazard assessment in San Ramón ravine, Santiago de Chile, from an engineering geological approach. *Environmental Earth Sciences*, 60(6), 1227–1243. <https://doi.org/10.1007/s12665-009-0264-5>.
- Lara, M., Sepúlveda, S., Celis, C., Rebolledo, S. and Ceballos, P. (2018) Landslide susceptibility maps of Santiago city Andean foothills, Chile. *Andean Geology*, 45(3), 433–442. <https://doi.org/10.5027/andgeoV45n3-3151>.
- Livneh, B., Rosenberg, E., Lin, C., Nijssen, B., Mishra, V., Andreadis, K. and Lettenmaier, D. (2013) A long-term hydrologically based dataset of land surface fluxes and states for the conterminous United States: update and extensions. *Journal of Climate*, 26(23), 9384–9392. <https://doi.org/10.1175/JCLI-D-12-00508.1>.
- López-Moreno, J., Navarro-Serrano, F., Azorín-Molina, C., Sánchez-Navarrete, P., Alonso-González, E., Rico, I., et al. (2018) Air and wet bulb temperature lapse rates and their impact on snowmaking in a Pyrenean ski resort. *Theoretical and Applied Climatology*, 135, 1–13. <https://doi.org/10.1007/s00704-018-2448-y>.
- Lundquist, J. and Cayan, D. (2007) Surface temperature patterns in complex terrain: daily variations and long-term change in the Central Sierra Nevada, California. *Journal of Geophysical Research: Atmospheres*, 112(D11124). <https://doi.org/10.1029/2006JD007561>.
- Lundquist, J., Neiman, P., Martner, B., White, A., Gottas, D. and Ralph, F. (2008) Rain versus snow in the Sierra Nevada, California: comparing Doppler profiling radar and surface observations of melting level. *Journal of Hydrometeorology*, 9(2), 194–211. <https://doi.org/10.1175/2007JHM853.1>.
- Maldonado, I., Ruiz, R. and Fuentes, M. (2010) *Manual de Instalación de Estaciones Automáticas*. Gobierno de Chile: INIA.
- Meza, F., Wilks, D., Gurovich, L. and Bambach, N. (2012) Impacts of climate change on irrigated agriculture in the Maipo Basin, Chile: reliability of water rights and changes in the demand for irrigation. *Journal of Water Resources Planning and Management*, 138(5), 421–430. [https://doi.org/10.1061/\(ASCE\)WR.1943-5452.0000216](https://doi.org/10.1061/(ASCE)WR.1943-5452.0000216).
- Minder, J., Mote, P. and Lundquist, J. (2010) Surface temperature lapse rates over complex terrain: lessons from the Cascade Mountains. *Journal of Geophysical Research: Atmospheres*, 115 (D14122) <https://doi.org/10.1029/2009JD013493>.
- Montecinos, A. and Aceituno, P. (2003) Seasonality of the ENSO-related rainfall variability in Central Chile and associated circulation anomalies. *Journal of Climate*, 16(2), 281–296. [https://doi.org/10.1175/1520-0442\(2003\)016<0281:SOTERR>2.0.CO;2](https://doi.org/10.1175/1520-0442(2003)016<0281:SOTERR>2.0.CO;2).
- Muñoz, R. 2005. ‘Characterization of the stability in the atmospheric boundary layer of Santiago Valley (Chile)’
- Muñoz, R. and Undurraga, S. (2010) Daytime mixed layer over the Santiago Basin: description of two years of observations with a lidar ceilometer. *Journal of Applied Meteorology and Climatology*, 49(8), 1728–1741. <https://doi.org/10.1175/2010JAMC2347.1>.
- Oertel, M., Meza, F.J. and Gironás, J. (2020) Observed trends and relationships between ENSO and standardized hydrometeorological drought indices in Central Chile. *Hydrological Processes*, 34 (2), 159–174. <https://doi.org/10.1002/hyp.13596>.
- Ojha, R. (2017) Assessing seasonal variation of near surface air temperature lapse rate across India. *International Journal of Climatology*, 37(8), 3413–3426. <https://doi.org/10.1002/joc.4926>.
- Ojha, R. (2019) Identification of homogeneous regions of near surface air temperature lapse rates across India. *International Journal of Climatology*, 39(11), 4288–4304. <https://doi.org/10.1002/joc.6073>.

- Otto-Bliesner, B., Marshall, S., Overpeck, J., Miller, G. and Hu, A. (2006) Simulating Arctic climate warmth and icefield retreat in the last interglaciation. *Science*, 311(5768), 1751–1753. <https://doi.org/10.1126/science.1120808>.
- Pages, M., Pepin, N. and Miró, J. (2017) Measurement and modeling of temperature cold pools in the Cerdanya valley (Pyrenees), Spain. *Meteorological Applications*, 24(2), 290–302. <https://doi.org/10.1002/met.1630>.
- Pávez, E., Lobos, G. and Jaksic, M. (2010) Long-term changes in landscape and in small mammal and raptor assemblages in Central Chile. *Revista Chilena de Historia Natural*, 83(1), 99–111. <https://doi.org/10.4067/S0716-078X2010000100006>.
- Peel, M., Finlayson, B. and McMahon, T. (2007) Updated world map of the Köppen-Geiger climate classification. *Hydrology and Earth System Sciences Discussions*, 4(2), 439–473. <https://doi.org/10.5194/hessd-4-439-2007>.
- Pellicciotti, F., Ragetti, S., Carenzo, M. and McPhee, J. (2014) Changes of glaciers in the Andes of Chile and priorities for future work. *Science of the Total Environment*, 493, 1197–1210. <https://doi.org/10.1016/j.scitotenv.2013.10.055>.
- Pepin, N. (2001) Lapse rate changes in northern England. *Theoretical and Applied Climatology*, 68(1–2), 1–16. <https://doi.org/10.1007/s007040170049>.
- Pepin, N. and Losleben, M. (2002) Climate change in the Colorado Rocky Mountains: free air versus surface temperature trends. *International Journal of Climatology: A Journal of the Royal Meteorological Society*, 22(3), 311–329. <https://doi.org/10.1002/joc.740>.
- Pérez, J. (2011) Riesgo de Inundación Producto del Cambio Climático Caso de Estudio: Quebrada San Ramón. (Undergraduate's thesis). Available at: Repositorio Académico Universidad de Chile (<http://repositorio.uchile.cl/handle/2250/104319>). Universidad de Chile
- Petersen, L. and Pellicciotti, F. (2011) Spatial and temporal variability of air temperature on a melting glacier: atmospheric controls, extrapolation methods and their effect on melt modeling, Juncal Norte glacier, Chile. *Journal of Geophysical Research: Atmospheres*, 116(D23109). <https://doi.org/10.1029/2011JD015842>.
- Pike, G., Pepin, N. and Schaefer, M. (2013) High latitude local scale temperature complexity: the example of Kevo Valley, Finnish Lapland. *International Journal of Climatology*, 33(8), 2050–2067. <https://doi.org/10.1002/joc.3573>.
- Prentice, I., Cramer, W., Harrison, S., Leemans, R., Monserud, R. and Solomon, A. (1992) A global biome model based on plant physiology and dominance, soil properties and climate. *Journal of Biogeography*, 117–134, 117. <https://doi.org/10.2307/2845499>.
- Programa Hidrológico Internacional para América Latina y el Caribe (PHI-LAC), 2013. *Curvas Intensidad Duración Frecuencia para las regiones Metropolitana, Maule y Biobío*. Intensidades desde 15 minutos a 24 horas. Documento técnico N°29, UNESCO PHI, 129 p.
- Rolland, C. (2003) Spatial and seasonal variations of air temperature lapse rates in alpine regions. *Journal of Climate*, 16(7), 1032–1046. [https://doi.org/10.1175/1520-0442\(2003\)016<1032:SASVOA>2.0.CO;2](https://doi.org/10.1175/1520-0442(2003)016<1032:SASVOA>2.0.CO;2).
- Romero, H., Ihl, M., Rivera, A., Zalazar, P. and Azocar, P. (1999) Rapid urban growth, land-use changes and air pollution in Santiago, Chile. *Atmospheric Environment*, 33(24–25), 4039–4047. [https://doi.org/10.1016/S1352-2310\(99\)00145-4](https://doi.org/10.1016/S1352-2310(99)00145-4).
- Roney, J. (2007) Statistical wind analysis for near-space applications. *Journal of Atmospheric and Solar-Terrestrial Physics*, 69 (13), 1485–1501. <https://doi.org/10.1016/j.jastp.2007.05.005>.
- Sanzana, P., Gironás, J., Braud, I., Muñoz, J., Vicuña, S., Reyes-Paecke, S., et al. (2019) Impact of urban growth and high residential irrigation on streamflow and groundwater levels in a Peri-urban semiarid catchment. *Journal of the American Water Resources Association*, 55(3), 720–739. <https://doi.org/10.1111/1752-1688.12743>.
- Sarmiento, C., Molina, M. and Jaque, J. (2019) Emergencias en los servicios sanitarios chilenos. Análisis técnico-regulatorio a la luz de los eventos de turbiedad extrema. *Revista de Derecho Administrativo Económico*, 27, 167–193. <https://doi.org/10.7764/redae.27.8>.
- Scharffenberg, W. and Fleming, M. (2010) *Hydrologic modeling system HEC-HMS user's manual*. Washington, DC: User Manual, USACE 306 p.
- Sepúlveda, S. and Padilla, C. (2008) Rain-induced debris and mudflow triggering factors assessment in the Santiago cordilleran foothills, Central Chile. *Natural Hazards*, 47(2), 201–215. <https://doi.org/10.1007/s11069-007-9210-6>.
- Sernageomin. (2007) *Principales desastres ocurridos desde 1980 en Chile*. Gobierno de Chile. Ministerio de Minería.
- SISS (Superintendencia de Servicios Sanitarios). (2018) *Informe de Gestión del Sector Sanitario 2018*. Gobierno de Chile. Ministerio de Obras Públicas.
- Tang, Z. and Fang, J. (2006) Temperature variation along the northern and southern slopes of Mt. Taibai, China. *Agricultural and Forest Meteorology*, 139(3–4), 200–207. <https://doi.org/10.1016/j.agrformet.2006.07.001>.
- Valenzuela, R. and Garreaud, R. (2019) Extreme daily rainfall in Central-Southern Chile and its relationship with low-level horizontal water vapor fluxes. *Journal of Hydrometeorology*, 20, 1829–1849. <https://doi.org/10.1175/JHM-D-19-0036.s1>.
- Viale, M. and Garreaud, R. (2014) Summer precipitation events over the western slope of the subtropical Andes. *Monthly Weather Review*, 142, 1074–1092. <https://doi.org/10.1175/MWR-D-13-00259.1>.
- Viale, M. and Garreaud, R. (2015) Orographic effects of the subtropical and extratropical Andes on upwind precipitating clouds. *Journal of Geophysical Research Atmosphere*, 120, 4962–4974. <https://doi.org/10.1002/2014JD023014>.
- Viale, M., Valenzuela, R., Garreaud, R. and Ralph, F. (2018) Impacts of atmospheric rivers on precipitation in southern South America. *Journal of Hydrometeorology*, 19, 1671–1686. <https://doi.org/10.1175/JHM-D-18-0006.1>.
- Wang, G., Zhao, M., Kang, M., Xing, K., Wang, Y., Xue, F. and Chen, C. (2017) Diurnal and seasonal variation of the elevation gradient of air temperature in the northern flank of the western Qinling Mountain range, China. *Journal of Mountain Science*, 14(1), 94–105. <https://doi.org/10.1007/s11629-016-4107-z>.
- White, A., Gottas, D., Strem, E., Ralph, F. and Neiman, P. (2002) An automated brightband height detection algorithm for use with Doppler radar spectral moments. *Journal of Atmospheric and Oceanic Technology*, 19(5), 687–697. [https://doi.org/10.1175/1520-0426\(2002\)019<0687:AABHDA>2.0.CO;2](https://doi.org/10.1175/1520-0426(2002)019<0687:AABHDA>2.0.CO;2).
- Yang, Z., Hanna, E. and Callaghan, T. (2011) Modelling surface-air-temperature variation over complex terrain around Abisko, Swedish Lapland: uncertainties of measurements and models at

- different scales. *Geografiska Annaler: Series A, Physical Geography*, 93(2), 89–112. <https://doi.org/10.1111/j.1468-0459.2011.00005.x>.
- Yáñez-Morróni, G., Gironás, J., Caneo, M., Delgado, R. and Garreaud, R. (2018) Using the weather research and forecasting (WRF) model for precipitation forecasting in an Andean region with complex topography. *Atmosphere*, 9(8), 304. <https://doi.org/10.3390/atmos9080304>.
- Zegpi, M. and Fernandez, B. (2010) Hydrological model for urban catchments—analytical development using copulas and numerical solution. *Hydrological Sciences Journal*, 55(7), 1123–1136. <https://doi.org/10.1080/02626667.2010.512466>.

## SUPPORTING INFORMATION

Additional supporting information may be found online in the Supporting Information section at the end of this article.

**How to cite this article:** Ibañez M, Gironás J, Oberli C, Chadwick C, Garreaud RD. Daily and seasonal variation of the surface temperature lapse rate and 0°C isotherm height in the western subtropical Andes. *Int J Climatol*. 2020;1–20. <https://doi.org/10.1002/joc.6743>